

Influence of Hydrogen Bonds and π – π Interactions on the Fluorescence of Crystalline (*N*-Alkylpyridyl)enamino-pyrrolo[2,3-*b*]quinoxalin-2-one Derivatives

Katarzyna Ostrowska,* Katarzyna M. Stadnicka, Marlena Gryl, Oskar Klimas, Mateusz Z. Breła, Piotr Goszczycki, Michał Liberka, Jarosław Grolik, and Agnieszka Węgrzyn



Cite This: *Cryst. Growth Des.* 2022, 22, 1571–1582



Read Online

ACCESS |



Metrics & More

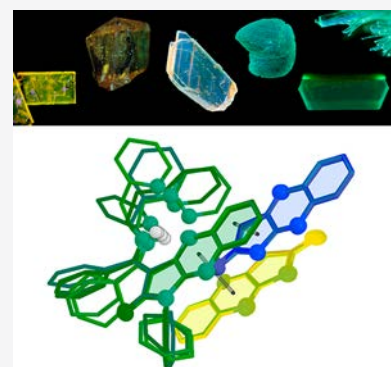


Article Recommendations



Supporting Information

ABSTRACT: This paper presents the relationship between the fluorescent properties of (*E/Z*)-(*N*-alkylpyridyl)enamino-pyrrolo[2,3-*b*]quinoxalin-2-one derivatives in the crystalline state and the molecular packing governed by the conformation of the molecules, hydrogen bonding, and π – π interactions. In particular, the type of 2-pyridyl alkyl chain (2-Py(CH₂)_{*n*} with *n* = 0,1,2) is responsible for the molecular packing and influences the fluorescence properties of crystalline pyrrolo[2,3-*b*]quinoxalines. The molecules studied exhibit permanent dipole moments that, in the crystalline phases, promote either the formation of dimers with an antiparallel orientation or stacks with a parallel dipole moment orientation. In dimers and stacks, the main observed interaction is the π – π type. The conformations of both (*E*)- and (*Z*)-enamines are stabilized by intramolecular hydrogen bonds from the NH group of the enamine to either the nitrogen atom N4 of the quinoxaline (*E*)-diastereoisomer or the oxygen atom of the amide carbonyl group in the (*Z*)-diastereoisomer. When an additional intramolecular hydrogen bond from the enamine NH group to the pyridyl nitrogen atom forms, it affects the conformation of the molecules, causing the reorientation of the molecular permanent dipole moment. Density functional theory (DFT) calculations performed for two neighboring molecules in dimers or stacks indicate two charge transfer mechanisms: intra- and intermolecular mechanisms. For centrosymmetric dimers, charge transfer occurs within each component molecule (intramolecular charge transfer). For stacks with molecules arranged by translation and noncentrosymmetric dimers, charge transfer is of an intermolecular nature. Higher absolute fluorescence quantum yields (Φ_f = 12.06–13.77%) are exhibited by the (*E*-diastereoisomers, which contain methylene or ethylene chains and form either translational stacks of the molecules or noncentrosymmetric dimers. The lowest absolute fluorescence quantum yields (Φ_f = 3.80–4.00%) are typical for the centrosymmetric dimers present in crystalline (*Z*)-(*N*-pyridyl)enamino-pyrrolo[2,3-*b*]quinoxaline and (*E*)-(*N*-ethylpyridyl)enamino-pyrrolo[2,3-*b*]quinoxaline. The fluorescence lifetimes τ were determined for single crystals of the studied phases (from 13.3 to 15.6 ns) and revealed one single process of radiative energy transfer.



1. INTRODUCTION

Single crystals of π -conjugated fused heteroaromatic systems have become an important target of research aimed at determining the relationship between the structure and the fluorescence of crystalline molecular materials^{1,2} as well as the charge transport in organic semiconductors.^{3,4} The properties of the crystals are closely associated with both their molecular packing and the electronic properties of the parent molecules. The shape of the assembled molecules and their short-range intermolecular interactions have a key influence on the packing in molecular crystals. According to the dense-packing theory, when “bumps and hollows” in the shapes of adjacent molecules fit together to form a periodic crystal structure, intermolecular contacts among organic molecules are maximized and void spaces are minimized.^{5,6} The mutual arrangement of the molecules is conditioned and stabilized by directional and nondirectional interactions due to Coulombic forces. Among directional interactions, hydrogen bonds have a pivotal role in

the stabilization of the crystal structures and influence the conformation of the parent molecules.⁷ Intramolecular hydrogen bonds restrict the vibration and rotation of a molecule, making its conformation more rigid. These phenomena are crucial for molecular solid-state fluorescence enhancement.^{8,9} Noncovalent interactions such as dispersion (London dispersion forces¹⁰) and van der Waals repulsion are responsible for π – π interactions. For dimers, the interactions may be regarded as attractive interactions of electrical quadrupoles, which overpower the repulsion of π -electron clouds.¹¹

Received: August 19, 2021

Revised: February 11, 2022

Published: February 21, 2022



Electron-donor and electron-acceptor substituents^{12–14} or heteroatoms inserted into aromatic hydrocarbon skeletons¹⁵ change the charge distribution in π -conjugated systems and generate a permanent dipole moment. The appearance of additional electrostatic dipole–dipole (Keesom forces¹⁶) and dipole–induced dipole (Debye forces¹⁶) interactions between component monomers results in the formation of relatively strong π – π interactions in dimers that decrease the interlayer distance between monomers.¹⁵

The relative orientation of π -conjugated fluorophores, including the area of π -overlap and the intermolecular distance in the dimers, strongly influences the solid-state fluorescence emission enhancement. In general, increasing the distance between π -stacking molecules and decreasing the π -overlap in the molecule can facilitate fluorescence via limiting exciplex or excimer formation in the excited states, which usually results in the dynamic quenching of emission.¹⁷

Our previous studies have shown the correlation between the crystal structure and photophysical properties of (*E*)-(N-alkyl-2-thienyl)enamino-pyrrolo[2,3-*b*]quinoxalin-2-one derivatives,¹⁸ where the 2-thienyl group controls the arrangement of monomers, dimers, and stacks of dimers in the appropriate crystal structures due to weak CH– π and S– π interactions. Here, we present the impact of the 2-pyridyl alkyl chain Py(CH₂)_{*n*} for *n* = 0, 1, or 2 on the solid-state fluorescence enhancement of (*E/Z*)-(N-alkylpyridyl)enamino-pyrrolo[2,3-*b*]quinoxalin-2-one derivatives in the crystalline state, which were tuned by intramolecular hydrogen bonds and π – π interactions. The alkyl linker and pyridyl group induce the specific mutual orientation of the enamino-pyrroloquinoxaline systems in the crystal structure and the π – π interactions between molecules in either dimers or stacks. The nitrogen atom of the pyridyl group allows the formation of an additional intramolecular hydrogen bond (N–H···N_{py}) apart from N–H···N₄(N_{Qui}), affecting the conformation of the molecules. *Ab initio* calculations¹⁹ and the subsequent quantum theory of atoms in molecules (QTAIM) analysis^{20,21} confirmed the existence of the aforementioned interactions and their influence on the fluorescence properties of the studied crystalline phases.

2. METHODS AND MATERIALS

2.1. Ultraviolet–Visible (UV–Vis), Fluorescence, and Infrared (IR) Spectra. UV–vis diffuse reflectance spectra of the single crystals of (*Z*)-2(*P*₂₁/*c*), (*E*)-2(*P*₂₁), (*E*)-3(*P*₂₁/*n*), (*E*)-4(*P*₂₁), (*E*)-4(*Cc*), and (*E*)-4(*P* $\bar{1}$) were recorded in the range of 190–900 nm using an Evolution 600 (Thermo) spectrophotometer. To obtain high-quality spectra, the following parameters were used: a resolution of 2 nm, a bandwidth of 4 nm, and a scan speed of 60 nm/min. The fluorescence measurements for (*Z*)-2(*P*₂₁/*c*), (*E*)-2(*P*₂₁), (*E*)-3(*P*₂₁/*n*), (*E*)-4(*P*₂₁), (*E*)-4(*Cc*), and (*E*)-4(*P* $\bar{1}$) were carried out using a Hitachi F-4500 spectrofluorometer. All solid-state spectra were recorded at 25 °C with an excitation slit width of 2.5 nm, an emission slit of 2.5 nm, and a 600 V photomultiplier tube voltage. IR spectra were recorded on a Thermo Scientific Nicolet IR200 Fourier transform infrared spectrometer.

2.2. X-ray Diffraction Measurements. Crystals of (*E*)-3(*P*₂₁/*n*) and (*E*)-4(*P* $\bar{1}$) for X-ray diffraction (XRD) experiments were obtained from acetonitrile solutions by slow evaporation under ambient conditions. Diffraction data sets were collected for single crystals with a Rigaku SuperNova diffractometer (low-temperature Cryo-Jet device and an Atlas CCD detector) using Cu K α radiation for (*E*)-3 and Mo K α radiation for triclinic (*E*)-4. Data collection, cell refinement, and data reduction were performed using the CrysAlisPro program.²² The data collection and crystal structure refinement details

are summarized in the Supplementary Information. The SIR92 program was used to solve the structures with direct methods.²³ SHELXL2013 was used to refine the structures with full-matrix least-squares methods (*F*² values against all reflections and anisotropic displacement parameters for nonhydrogen atoms).²⁴ The positions of the hydrogen atoms (found from Fourier difference maps) were refined in the riding model with *U*(iso) = 1.2*U*(eq) of the parent atom. Graphical programs ORTEP-3 (operating under WinGX suite) and Mercury 2.3 were used to prepare the molecular graphics.^{25–27} The structural details for (*E*)-3 and (*E*)-4(*P* $\bar{1}$) were deposited in the Cambridge Structural Database at the Cambridge Crystallographic Data Centre under CCDC number 1519234 and 2086613, respectively.

2.3. Computational Details. The presented density functional theory (DFT) calculations concerning the dimer and the monomer structure were based on the Amsterdam Density Functional (ADF) program, ver. 2017.²⁸ The Becke–Perdew exchange–correlation functional^{29,30} was used together with the dispersion correction scheme by Grimme et al.³¹ A standard triple- ζ STO basis set with one set of polarization functions was used for all atoms. The relativistic effects were included at the scalar relativistic ZORA level of approximations,³² as implemented in the ADF package. The bonding between two monomers in the dimeric structures was analyzed with the ETS bond energy decomposition scheme.³³ In this approach, the overall bonding energy (ΔE_{tot}) is decomposed into the electrostatic interaction energy (ΔE_{elstat}) between the frozen charge distributions of the two distorted fragments as they are brought together, the repulsive interaction between occupied orbitals on the two monomers (Pauli, ΔE_{Pauli}), the stabilizing dispersion interaction between the two fragments (E_{disp}), and the orbital stabilization term (ΔE_{orb}) that allows us to analyze the virtual orbitals on both monomers in the dimeric structure, which participate in the bonding, as a change in the density ($\Delta\rho$).³⁴

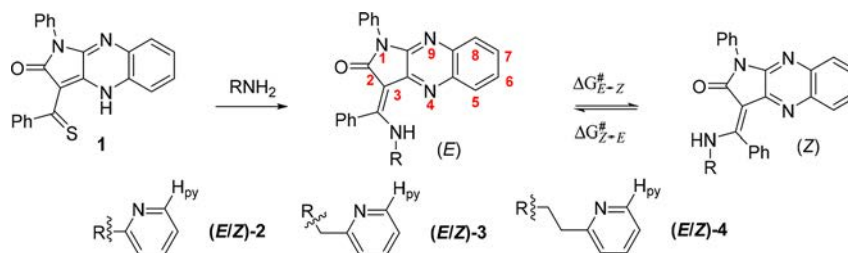
Additionally, the time-dependent density functional theory (TD-DFT) calculations^{35,36} for dimer structures were performed in the ADF package. To visualize the transition, natural transition orbitals (NTO) were analyzed.³⁷

The approximation of the solid-state spectroscopic features of the considered crystal structure was based on CP2k.³⁸ TD-DFT calculations were performed to consider the excited states.³⁹ The Becke–Lee–Yang–Parr (BLYP) functional was used as the exchange–correlation functional with Grimme’s dispersion corrections (D3).^{31,40,41} Periodic boundary conditions (PBCs) were used to approximate the crystal field. A mix of double- ζ valence-polarized (DZVP) basis sets and plane waves (cutoff of 450 Ry) was used. The trajectory was visualized and analyzed by VMD software.⁴² The DFT calculations performed for (*E*)-4(*P*₂₁) considered the presence of the water molecule.

2.4. Fluorescence Quantum Yield and Lifetime. Absolute luminescence quantum yields (Φ_f) were determined by the direct excitation method using an integrating sphere module and barium sulfate as the reference material. An F55 spectrofluorometer (Edinburgh Instruments) equipped with a Xe (150 W) arc lamp was used as an excitation source, and a Hamamatsu photomultiplier of the R928P type was used as a detector. Emission lifetime measurements were conducted on an F55 spectrofluorometer using a time-correlated single photon counting method with an EPLED-380 (Edinburgh Instruments) picosecond pulsed light emitting laser diode (374.4 nm).

3. RESULTS AND DISCUSSION

3.1. Synthesis and UV Data in Solution. The syntheses of push–pull chromophores (*E/Z*)-2,⁴³ (*E/Z*)-3,⁴⁴ and (*E/Z*)-4⁴⁵ were published earlier, and the crystal structures of compounds (*Z*)-2, (*E*)-2, (*E*)-4(*P*₂₁), and (*E*)-4(*Cc*) are available in the Cambridge Structural Database under REFCODs LUYWAF, LUYJIA, KOPZEW, and KOPZAF, respectively. The synthetic procedure for the new phase, namely (*E*)-3(*P*₂₁/*n*) and (*E*)-4(*P* $\bar{1}$), was based on the

Scheme 1. Synthesis and *E/Z* Isomerization of Enamines^{a,43–45}

^aH_{py} was marked because of its important signal in the ¹H NMR data.

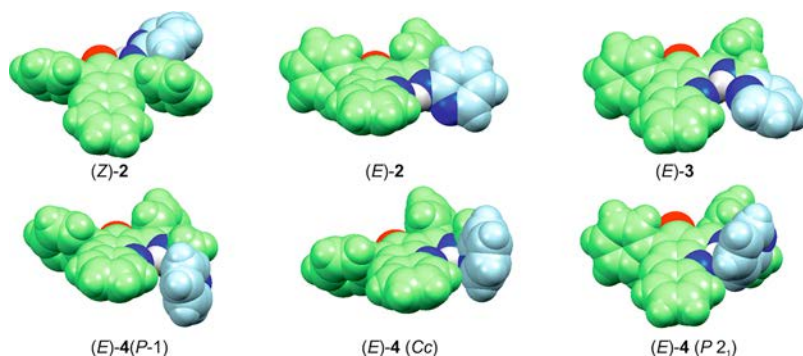


Figure 1. Enamine molecules drawn with the space-filling model (Table S5).

enamination of 3-thiobenzoylpyrrolo[2,3-*b*]quinoxaline with an excess amount of 2-alkylaminopyridine in propan-1-ol⁴⁶ (Scheme 1).

The compounds occur in the equilibrium of (*E*)- and (*Z*)-diastereoisomers,^{47,48} with the *E*-form predominating in the solutions. As a result of *E/Z*-isomerization, the enamines exhibit very weak dual fluorescence ($\Phi_f < 0.1\%$) in organic solvents.⁴⁹ The spectral properties (UV–vis, fluorescence, and ¹H NMR spectra) of enamines (*E/Z*)-2, (*E/Z*)-3, and (*E/Z*)-4 in solutions are described in the SI (Table S1 and Figures S1–S3).

3.2. Crystal Structure and QTAIM Analysis. During the crystallization processes, the *E/Z*-equilibrium of the enamines shifted to the *E*-isomer for (*E*)-2(*P*₂₁),⁴³ (*E*)-3(*P*₂₁/*n*), (*E*)-4(*P*₂₁),⁴⁵ (*E*)-4(*Cc*),⁴⁵ and (*E*)-4(*P*₁). Single crystals of (*E*)-2(*P*₂₁) were isolated from either MeOH or dimethyl sulfoxide (DMSO)-*d*₆; those of (*E*)-3(*P*₂₁/*n*) were isolated from DMSO-*d*₆; and those of the three conformational polymorphs⁵⁰ with ethyl-(2-pyridyl) groups, namely (*E*)-4(*P*₁), (*E*)-4(*P*₂₁), and (*E*)-4(*Cc*), were isolated from CH₃CN, CH₃CN with several added water droplets, and a 50% water–acetonitrile solution, respectively. The diastereoisomer (*Z*)-2(*P*₂₁/*c*) was isolated from solution in CH₃CN upon exposure to daylight. The data collection, crystal structure refinement, and structural analysis details for two new crystal structures, *i.e.*, monoclinic (*E*)-3(*P*₂₁/*n*) and triclinic (*E*)-4(*P*₁), are summarized in the Supporting Information (Tables S2–S4 and Figures S4–S9). X-ray crystal structure analysis for the single crystals of (*Z*)-2(*P*₂₁/*c*), (*E*)-2(*P*₂₁), (*E*)-3(*P*₂₁/*n*), (*E*)-4(*P*₂₁), (*E*)-4(*Cc*), and (*E*)-4(*P*₁) revealed that all the molecules exhibited planar chirality, either *pS* or *pR*, and formed either dimers or stacks with molecules of the same or opposite chirality depending on the space group symmetry. The absolute configurations *pR* and *pS* for the molecules were assigned according to the CIP rules.⁵¹ The pyrroloquinoxaline heterocyclic system defines the planar

chirality of the molecules, whereas the nitrogen atom of the pyridyl group acts as the pivot atom. The molecules drawn with the space-filling model are shown in Figure 1.

Racemic aggregates (*Z*)-2(*P*₂₁/*c*) contain a pair of enantiomers, *pR* and *pS*, in a head-to-tail arrangement, a gravity center distance of the pyrroloquinoxaline heterocyclic system from Cg7 to Cg7' (for the molecules related by the center of symmetry) equal to 3.844 Å, and a π – π interplanar separation of 3.668 Å. The single crystals of (*E*)-2(*P*₂₁) exclusively include either the *pR* or *pS* configuration of the molecules, forming translational stacks of dimers. The dimer is formed by molecules with a parallel mutual orientation in a head-to-tail fashion following a twofold screw axis and a π – π separation of 3.287 Å. Here, the Cg7–Cg7' distance is equal to 3.654 Å and the offset distance is 1.596 Å. Enamine (*E*)-3 crystallizes in the monoclinic system following space group *P*₂₁/*n* (the crystal structure is centrosymmetric). The racemic structure of the (*E*)-3 crystals contains molecules with both *pS* and *pR* configurations in a 1:1 ratio. Each enantiomer forms a separate stacking arrangement along [010] in a face-to-face fashion due to π – π interactions between the benzene and pyrrole rings of the adjacent pyrroloquinoxaline systems, with distances from Cg3 (the benzene gravity center) to Cg1' (the gravity center of the pyrrole ring moved by *b*) of 3.527 Å. In the noncentrosymmetric crystal structure of (*E*)-4(*P*₂₁), aggregates are formed in the same manner as those in the (*E*)-3 crystal structure, but stacks of *pS* and *pR* molecules are present in separate crystals. The compound crystallizes as a hydrate, and the water molecules stabilize the helical chirality of the molecular arrangements through hydrogen bonds, *M* for crystals built of *pS* molecules and *P* for crystals built of *pR* molecules. The stacks are governed by π – π interactions (3.411 Å) along [100]. The racemic single crystals (*E*)-4(*Cc*) contain chiral dimers formed by two symmetrically independent enamine molecules with the same configuration but two different conformations, *C* and *D*, due to the different

Table 1. Intramolecular Hydrogen Bond Geometry, Energy, and IR Data for the Studied Molecules in the Crystalline State

ID	space group and crystal system	experimental geometrical parameters of intramolecular hydrogen bonds D—H...A, D—H, H...A, and D...A (Å) and \angle DHA ($^{\circ}$)	$E_{\text{NH}\cdots\text{N}/\text{NH}\cdots\text{O}}$ (kcal/mol)	C=O stretching vibration (cm^{-1})
(Z)-2	$P2_1/c$ monoclinic	N—H...O=C, 0.90(1), 1.98(1), 2.715(1), 137(1)	−6.21	1661
(E)-2	$P2_1$ monoclinic	N—H...N _{Qui} , 0.91(1), 2.05(2), 2.839(3), 143(3)	−5.15	1695
(E)-3	$P2_1/n$ monoclinic	N—H...N _{Qui} , 0.89(1), 2.12(2), 2.813(4), 135(3)	−5.60	1693
		N—H...N _{py} , 0.89(1), 2.23(3), 2.688(4), 111(3)	−4.49	
(E)-4($P2_1$)	$P2_1$ monoclinic	N—H...N _{Qui} , 0.86(1), 2.12(2), 2.859(2), 143(2)	−4.33	1699
		N—H...N _{py} , 0.86(1), 2.25(2), 2.716(3), 114(2)	−4.30	
(E)-4(Cc)	Cc monoclinic	(C) N—H...N _{py} , 0.90(1), 2.22(2), 2.908(1), 134(1)	−5.32	1700
		(D) N—H...N _{py} , 0.89(1), 2.05(2), 2.811(1), 142(1)	−3.37	
		(D) N—H...N _{py} , 0.90(1), 2.42(2), 2.939(2), 117(1)	−2.43	
(E)-4($P\bar{1}$)	$P\bar{1}$ triclinic	N—H...N _{Qui} , 0.86(1), 2.15(1), 2.857(2), 139(2)	−4.46	1698

conformations of the ethylpyridyl chain. The molecules of the same enantiomer are arranged in a head-to-tail manner with a Cg7(C)–Cg7(D) distance of 3.507 Å and an offset distance of 0.687 Å, forming a chiral dimer. Another polymorph of (E)-4 crystallizes in the triclinic centrosymmetric space group $P\bar{1}$. The structure of (E)-4($P\bar{1}$) is built of centrosymmetric dimers formed by two molecules of opposite configurations, namely pS and pR, with a Cg7–Cg7' distance of 3.450 Å and an offset distance of 1.018 Å.

Single-crystal X-ray structure analysis indicated that enamines with an *E*-configuration are stabilized by the moderate intramolecular hydrogen bond between the enamine group NH and the nitrogen atom N(4) of the pyrazine ring in the quinoxaline system (*i.e.*, N_{Qui}), whereas the (*Z*)-diastereomer has an appropriate hydrogen bond between the enamine group NH and the amide carbonyl oxygen atom O(2). The formation of these hydrogen bonds imposes a planar conformation of the molecules that, in the cases of (E)-3($P2_1/n$), (E)-4($P2_1$), and (E)-4(Cc), is additionally stabilized by hydrogen bonds formed between the enamine NH and the nitrogen atom of the pyridyl substituent (N_{py}) (Tables 1 and S4). The presence of hydrogen bonds in CD₃CN solutions is also manifested by chemical shifts for the (*E/Z*)-NH proton and the (*E/Z*)-H_{py} proton at the C atom in the position adjacent to N_{py} (Table S1 and Figure S3c). The chemical shift value for the H_{py} proton also indicates the strength of the hydrogen bond between NH and N_{py} as the acceptor. The stronger the N—H...N_{py} hydrogen bond, the more deshielded the H_{py} proton, as the N_{py}–C–H_{py} bonds in the pyridyl substituent are more polarized. The (*E/Z*)-H_{py} protons appeared to be most deshielded in the case of (*E/Z*)-3, for which the formation of the intramolecular hydrogen bond N—H...N_{py} was detected even in solution. As the strength of this interaction increases, the conformation of the enamine substituent becomes more rigid, and the intramolecular vibrations and rotations become more restricted. By comparing the chemical shifts for the C(5)–H proton of the *E*- and *Z*-isomers, it is also possible to estimate the formation of an intramolecular hydrogen bond between NH and N_{Qui}, which is broken during the *E/Z*-interconversion in solution. In the lowest field range of the ¹H nuclear magnetic resonance (NMR) experiment, the C(5)–H proton was observed at 8.0, 7.97, and 7.76 ppm for (E)-2, (E)-3, and (E)-4, respectively (Figure S3).

To confirm the existence of the geometrically predicted inter- and intramolecular interactions responsible for the structural features, the QTAIM analysis was performed for dimers of the enamine (*E*)- and (*Z*)-diastereoisomers. The

calculations were performed for the dimers at the B3LYP/6311-G** level using the experimental geometry (Table 2 and Figures S10 and S11). The electron density, the Laplacian electron density, and the local kinetic and potential energy densities are given in Table S6. The energies for weak intermolecular interactions were estimated from the potential energy density using the approach described by Espinosa.⁵² Molecular graphs with the critical points marked for (E)-3 and (E)-4($P\bar{1}$) are shown in Figure S10.

A moderate hydrogen bond (N—H...O=C) was found for the (*Z*)-diastereoisomer (Z)-2 (−6.21 kcal/mol). The IR spectra of (Z)-2 show that the formation of the N—H...O hydrogen bond shifts the amide carbonyl stretching band to a lower frequency, *i.e.*, from 1695 cm^{−1} for the *E*-isomer to 1661 cm^{−1} for the *Z*-isomer (Table 2 and Figures S12–S16). The elongation of the linker between the pyridyl and enamine groups due to the methylene spacer facilitates the formation of bifurcated hydrogen bonds (N—H...N_{Qui} and N—H...N_{py}) and slightly increases the energy of the N—H...N_{Qui} bond of the *E*-isomer from −5.15 kcal/mol for (E)-2 to −5.60 kcal/mol for (E)-3. The energy for N—H...N_{py} is equal to −4.49 kcal/mol. The ethylene linker also facilitates the formation of bifurcated hydrogen bonds, but because of the more labile conformation the formation of bifurcated hydrogen bonds does not significantly affect the bond strength or energy value in the case of polymorphs (E)-4($P2_1$) and (E)-4(Cc) (Table 2).

The presence of intramolecular bifurcated hydrogen bonds (N—H...N_{Qui} and N—H...N_{py}) additionally stabilizes the conformation and facilitates the planarization of the molecule (Figure 1). The mutual antiparallel orientation of chromophores is caused by dipole–dipole interactions between molecules with permanent dipole moments (Table 2 and Figure S11). Chromophores in dimers and stacks are arranged in either a head-to-tail or head-to-head manner, with a parallel alignment in either case. The energy of π – π interactions between molecules in the dimers, which were cut from the crystal structure and taken without further optimization of the geometry, as assessed by QTAIM analysis are given in Tables 2 and S6.

The energy of the π – π interaction was estimated by QTAIM analysis to be −3.13 kcal/mol for dimer (Z)-2, with a head-to-tail orientation, an interplanar distance of 3.668 Å, and an overlapping fraction of fluorophore surface area (fso) of 66%.⁵³ (Table 2). Among the enamino-pyrroloquinoxalines with the *E*-configuration, the lowest energies were found for (E)-3 and (E)-4($P2_1$) as −3.39 and −4.01 kcal/mol, fso values of 29% and 35%, and interplanar distances of 3.527 and 3.411 Å, respectively. In the case of dimers with molecules oriented

Table 2. Geometric Parameters and Spectral Properties of Enamine for Isolated Single Crystals (*Z*)-2, (*E*)-2, (*E*)-3, (*E*)-4(*P*2₁), (*E*)-4(*Cc*), and (*E*)-4(*P*1̄).^a

Drawing of enamine dimer/stack in single crystal structure ^b	ID/ space group/ arrangement of molecules	π - π / Cg-Cg' Distance/ off-set [Å]	Dipole ^c moment: monomer/ dimer/ trimer [D]	E(π - π) [kcal/mol]/ Fraction of π - π overlapping surface [%]	Emission $\lambda_{ex}/\lambda_{em}$ [nm]/ Absorption ^d λ_{max} [nm]/ Stokes shift [cm ⁻¹]	Φ_f^e ($\lambda_{ex}=374$ / 360 nm) [%]	Fluorescence Lifetimes ^f τ / k_f / k_{nr} [ns]/[s ⁻¹]
	(Z)-2 <i>P</i> 2 ₁ / <i>c</i> centrosym. dimer head-to-tail	3.668/ Cg7-Cg7' 3.844/ 0.725	4.86/ 0.00	-3.13/66%	440/542/ 428/ 4914	3.80/1.97	14.8 (±0.12) /0.0025 /0.065
	(E)-2 <i>P</i> 2 ₁ stack of dimer head-to-tail	3.287/ Cg2-Cg3' 3.654/ 1.357	4.73/ 2.90/ 5.86	-5.42/40%	440/505/ 461/ 1890	8.49/5.17	14.4 (±0.15) /0.0059 /0.063
	(E)-3 <i>P</i> 2 ₁ / <i>n</i> translational stack head-to-head	3.527/ Cg1-Cg3' 3.602/ 1.069	7.48/ 14.77/ 20.55	-3.39/ 29%	430/491/ 420/ 3443	12.06/18.50	13.3 (±0.09) /0.0090 /0.066
	(E)-4(<i>P</i> 2₁) , translational stack head-to-head	3.411/ Cg1-Cg3' 3.515/ 0.865	3.77/ 7.01/ 10.45	-4.01/35%	430/480/ 401/ 4104	13.77/6.93	15.6 (±0.16) /0.0088 /0.055
	(E)-4(<i>Cc</i>) non-centrosym. dimer head-to-tail	3.439/ Cg1-Cg3' 3.507/ 0.687	6.57/ 2.27	-6.03/67%	455/509/ 488/ 843	12.69/5.98	14.8 (±0.07) /0.0081 /0.059
	(E)-4(<i>P</i>-1) centrosym. dimer head-to-tail	3.449/ Cg2-Cg3' 3.597 1.018	5.18/ 0.00	-4.65/54%	360/460,551/ 354, 509/ 1112	4.00/5.87	15.3 (±0.15) /0.0026 /0.063

^a $\Phi_f(\lambda_{ex})$ represents the fluorescence quantum yields. Cg7 is the gravity center of the pyrroloquinoxaline fluorophore. Ring gravity centers for the fluorophore are as follows: Cg7 for N(1)C(2)C(3)C(3a)N(4)C(4a)C(5)C(6)C(7)C(8)C(8a)N(9)C(9a), Cg1 for N(1)C(2)C(3)C(3a)C(9a), Cg2 for C(3a)N(4)C(4a)C(8a)N(9)C(9a), and Cg3 for C(4a)C(5)C(6)C(7)C(8)C(8a). ^bOverlapping surfaces of fluorophores are marked in color. ^cDipole moments for the monomers, dimers, and trimers were calculated at the B3LYP-6311-G** level using experimental geometries of the molecules without optimization. ^dUV-vis spectra are included in the SI (Figures S27–S31). ^eFluorescence quantum yields for single crystals were determined by a direct excitation method using an integrating sphere and for powders using a procedure described previously⁵⁴ for $\lambda_{ex} = 360$. ^f $\lambda_{ex} = 374.2$ nm, k_f is the radiative rate constant, and k_{nr} is the nonradiative rate constant.

head-to-tail, a moderate π - π interaction (-6.03 kcal/mol) was observed for the noncentrosymmetric dimer (*E*)-4(*Cc*), with π - π distances of 3.439 Å and $f_{so} = 67\%$.

The shortest interplanar distance between chromophores (π - $\pi = 3.287$ Å) was observed for the (*E*)-2 dimer. This distance is smaller than both the sum of the van der Waals radii of the two sp^2 -hybridized carbon atoms and the 3.345 Å the

interlayer distance in graphite.⁷ In the (*E*)-2 dimer, the fraction of the overlapping surface area for the two pyrroloquinoxaline systems in the dimer is 40%, and the π - π interaction energy is -5.42 kcal/mol.

3.3. Density Functional Theory (DFT) Calculations. To shed additional light on the fluorescence properties of the studied crystals, the electron properties of the systems were

Table 3. Results of DFT Calculations for Monomers and Dimers and the ETS Analysis for the Considered Dimer Structures^a

ID	(Z)-2	(E)-2 ^{**}	(E)-3 [*]	(E)-4(P2 ₁) [*]	(E)-4(Cc)	(E)-4(P $\bar{1}$)
	P2 ₁ /c	P2 ₁	P2 ₁ /n	P2 ₁	Cc	P $\bar{1}$
space group						
DFT calculations for monomer (point group 1)						
Dipole moment (D)	4.70	4.62	7.45	5.21	5.84	5.14
HOMO (eV)	-5.552	-5.537	-5.241	-5.388	-5.328	-5.331
LUMO (eV)	-3.142	-3.081	-2.760	-3.187	-2.713	-2.713
HOMO–LUMO gap (eV)	2.410	2.456	2.481	2.211	2.615	2.618
DFT calculations for dimers						
ΔE_{Pauli}	20.32	26.63	18.52	29.73	26.16	20.45
ΔE_{el}	-9.56	-11.31	-7.38	-12.45	-10.1	-8.87
ΔE_{steric}	10.76	15.32	11.14	17.28	16.06	11.58
ΔE_{orb}	-5.65	-6.46	-5.44	-8.69	-7.06	-6.41
E_{disp}	-33.79	-30.02	-30.96	-40.26	-38.61	-34.56
ΔE_{tot}	-28.68	-21.16	-25.26	-31.67	-29.61	-29.46
dipole moment (D)	0.00	2.87	13.87	9.83	2.30	0.00
HOMO (eV)	-5.548	-5.539	-5.154	-5.547	-5.166	-5.217
LUMO (eV)	-3.218	-3.088	-2.882	-3.036	-2.782	-2.735
HOMO–LUMO gap (eV)	2.330	2.451	2.272	2.511	2.384	2.482
excitation energy (TD-DFT)	2.391	2.424	2.297	2.233	2.512	2.629
calculated absorption maximum (based on the excitation energy for the dimer) (nm)	519	511	540	555	494	471

^aEnergies are in kilocalories per mole. Note that in some structures there are stacks (*) or stacks of dimers (***) instead of the considered dimers. Total bonding energy was calculated as follows: $\Delta E_{\text{tot}} = \Delta E_{\text{Pauli}} + \Delta E_{\text{el}} + \Delta E_{\text{orb}} + E_{\text{disp}}$, where $\Delta E_{\text{el}} + \Delta E_{\text{Pauli}} = \Delta E_{\text{steric}}$.

calculated using density functional theory (DFT). The calculations were carried out based on the three molecular models for all studied systems: a single molecule, the dimer structure present in crystalline state, and the unit cell with periodic boundary conditions. The elucidation of the interaction patterns in the studied crystals was the main goal of the calculations presented. For this reason, the analysis was performed based on the geometries extracted from crystal structures. The DFT results for monomers and dimers are presented in Table 3, whereas the DFT results for the unit cell with periodic boundary conditions are given in Table S7. (E)-3(P2₁/n) has the largest dipole moment (7.45 D) (Figure S17), while (E)-4(P $\bar{1}$) has the largest HOMO–LUMO gap (2.618 eV). The representation of molecular orbitals (HOMO and LUMO) characteristic of the dimer of (E)-4(P $\bar{1}$) and a scheme showing the first three electronic transitions are shown in Figure S18. The calculated highest occupied molecular orbitals (HOMOs) and lowest unoccupied molecular orbitals (LUMOs) for the (Z)-2, (E)-2, (E)-4(P2₁), and (E)-4(Cc) dimers are presented in Figures S19–S22, respectively. The orientations of the dipole moments for (Z)-2, (E)-2, (E)-3, (E)-4(P2₁), (E)-4(Cc), and (E)-4(P $\bar{1}$) are shown in Figures S23–S25, respectively. After comparing all the HOMO–LUMO gaps and dipole moments, no strong correlation was elucidated. Electronic structure analysis of the dimers was performed based on energy decomposition analysis and extended transition state (ETS) analysis.

The interaction energy ranges from -21.16 kcal/mol for (E)-2(P2₁) to -31.67 kcal/mol for (E)-4(P2₁). The fluctuation of the interaction energy between the considered systems clearly originates from the dispersion energy, which ranges from -30.02 kcal/mol for (E)-2(P2₁) to -40.26 kcal/mol for (E)-4(P2₁). As discussed above, the mutual orientation of the single molecules is different in the studied systems. Let us compare two neighboring molecules in the stack of the (E)-3(P2₁/n) structure (related by head-to-head orientations) with the dimer in the (E)-4(P $\bar{1}$) structure (related by head-to-

tail orientations). The head-to-tail system has a dipole moment equal to zero because the dimer is centrosymmetric. Two molecules in the stack of (E)-3(P2₁/n) accumulate a dipole moment of 13.87 D. Unfortunately, considering only two neighboring molecules is not a good choice replicating interactions in stack systems. The tetramer model (four neighboring molecules in the stack) would be the better choice; however, that model has many disadvantages. First, analyzing the electron flow and understanding the relationship between the electronic structure and spectral properties is challenging. Second, all systems should be recalculated at the same size of the model systems, which would dramatically increase computational costs. However, an analysis of frontier orbitals of the dimer structures could provide knowledge on the charge transfer between molecules. The main differences between systems are elucidated in the sum (ΔE_{steric}) of the electrostatic energy (ΔE_{el}) and Pauli repulsion (ΔE_{Pauli}) terms. The lowest energies, and thus the weakest destabilization by Pauli repulsion, were observed for (Z)-2, (E)-3(P2₁/n), and (E)-4(P $\bar{1}$).

The orbital interaction energies (ΔE_{el}) of (E)-3(P2₁/n) and (E)-4(P $\bar{1}$) were visualized as deformation densities³³ in Figure 2a and b, respectively. The deformation densities visualize the charge flow based on calculations exclusively for a fragment of the structure, either for two molecules in the stack or for the dimer.²⁸ The deformation density for (E)-3(P2₁/n) elucidates the charge transfer between two neighboring monomers. The chromophore group participates in the charge transfer. Figure 2a depicts the charge flow from the top monomer to the bottom monomer. The charge flow observed for the dimer of (E)-4(P $\bar{1}$) is completely different. In that case, the charge flow is localized on each molecule of the dimer. There is strong polarization in the dimer structure, especially between the chromophore center and the phenyl substituent at N1 of pyrroloquinoxaline. Polarization is also indicated by the accumulation of a negative charge (red color) in the molecular electrostatic potential (MEP, Figure 2d). However, some

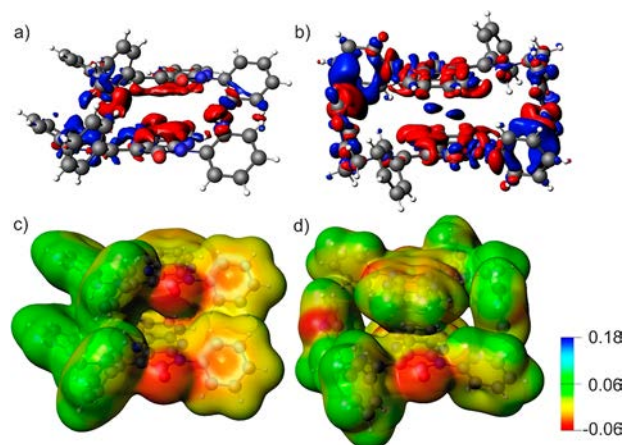


Figure 2. Deformation density $\Delta\rho$ ($\Delta\rho = \rho_{\text{dimer}} - (\rho_{\text{monomer}_1} + \rho_{\text{monomer}_2})$) for (a) two neighboring molecules in stack of (E)-3(P₂₁/n) and (b) the dimer of (E)-4(P₁). The blue color indicates the accumulation of electron density, and the color red indicates depletion. The molecular electrostatic potential (MEP) color-coded at the electron-density isosurface ($\rho = 0.002$ au) for (c) (E)-3(P₂₁/n) and (d) (E)-4(P₁). The color scale is indicated in the bottom-right corner of the figure.

relatively small attractive interactions can also be seen between monomers in (E)-4(P₁) (notice the accumulation of electron density in Figure 2b). The deformation density clearly shows the strong electronic conjugation between molecules in the dimer in the ground state for (E)-4(P₁) (see Figure 2b).

Figure 3 presents the first excitations in terms of NTO (Table S8, Figure S26) for (E)-4(P₁) and (E)-3(P₂₁/n). First,

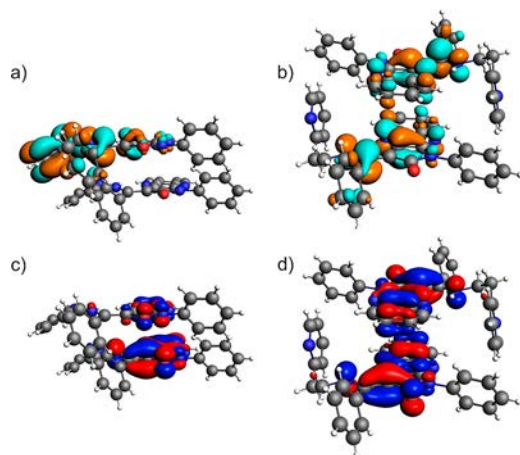


Figure 3. Natural transition orbitals (NTOs) for the first excitations. Panels a and b show the virtual orbitals, and panels c and d depict the occupied orbitals. Panels a and c depict the excitation for (E)-3(P₂₁/n), and panels b and d depict the first excitation for (E)-4(P₁).

the depicted orbitals are the major orbitals. The other NTO involved in this transition plays only a marginal role. The elucidated transitions are in line with the previous observation concerning the charge flow (Figure 2a and b). Excitation in (E)-4(P₁) is localized in the chromophore group, while excitation in (E)-3(P₂₁/n) spreads to the phenyl substituent at N1 of pyrroloquinoxaline.

Figures S18 and S17 depict the approximation of the electron transitions from the ground state to the three lowest unoccupied molecular orbitals for (E)-4(P₁) and

(E)-3(P₂₁/n), respectively. The HOMO orbital is mostly localized on one molecule; however, the LUMO orbitals are localized on the second molecule of the fragment of the stack taken for calculations. LUMO + 1 and LUMO + 2 orbitals are spread over the chromophore center and the pyridyl group. The frontier orbital analysis is in line with the deformation density calculations.

3.4. Fluorescence Properties of Single Crystals. As indicated before (Section 3.1), E/Z-interconversion, which is related to the rotation around the C(3)–C(30) bond of the zwitterion intermediate form, quenches the enamine fluorescence in solutions. In the solid state, conformational changes and vibrational motions are suppressed, and the rigidity of the structure leads to the radiative deactivation of the excited states. The single crystals of the studied enamines show fluorescence emissions with one band (Figure 4a) except for (E)-4(P₁), where two bands are present due to symmetry-forbidden (551 nm, Laporte rule) and symmetry-permitted (460 nm) transitions (Table 2 and Figure S27–31). For all crystalline enamines, red-shifts of the emission bands were observed at approximately 10–30 nm compared to those in acetonitrile solutions except for (E)-2 (the stack of dimers is present in its crystalline state), where a blue-shift was observed. The fluorescence quantum yields (Φ_f) were determined using two methods: a direct excitation method using integrating spheres (Table S9) for single crystals and the procedure described by Ware for the powdered samples mixed with KCl (Figure S32–S37). Single crystals of enamines exhibit higher absolute fluorescence quantum yields than the crystals of enamines in solutions. The lowest absolute fluorescence quantum yields are 3.80% and 4.00% for (Z)-2 and (E)-4(P₁), respectively. The highest yields of 12.06–13.77%, were exhibited by (E)-3, (E)-4(P₂₁), and (E)-4(Cc). For (E)-2, Φ_f amounts to 8.49% (Table 2). Some regularity can be noticed here. Centrosymmetric single crystals with head-to-tail dimers have lower fluorescence quantum yields than those with two molecules in stacks or dimers in non-centrosymmetric crystal structures. Considering the phenomenon described in the literature,^{55,56} we can conclude that similar fluorescence quantum yields were observed both for the powdered samples (diluted in KCl) and those determined for single crystals using the integrating sphere (absolute fluorescence quantum yields).

The measurements of fluorescence lifetimes for all studied compounds gave values from 13.3 to 15.6 ns and revealed one single process of radiative energy transfer in the crystalline state (Tables 2 and S10).

3.5. Discussion. The electron density distributions of HOMOs and LUMOs of the structures obtained by DFT calculations (Section 3.3) showed that the HOMOs were delocalized over the pyrroloquinoxalin-2-one system in the case of the head-to-head molecular stacking in (E)-3. However, the LUMOs were delocalized over only one of two molecules in the stack, with the maximum component on its pyridine ring. The calculations indicated that intermolecular charge transfer from both molecules of the dimer occurred to the pyridyl group of one component only. The pyridine ring is almost coplanar with the fluorophore core due to the N–H...N_{py} hydrogen bond, which enables both the extension of π -electron transfer and coupling between the heterocyclic moieties. The direction of the electron transfer is consistent with the orientation of the dipole moment. The value of the dipole moment estimated for one molecule (monomer) is 7.45 D, that for two molecules in the stack is 13.87 D (Table 3 and

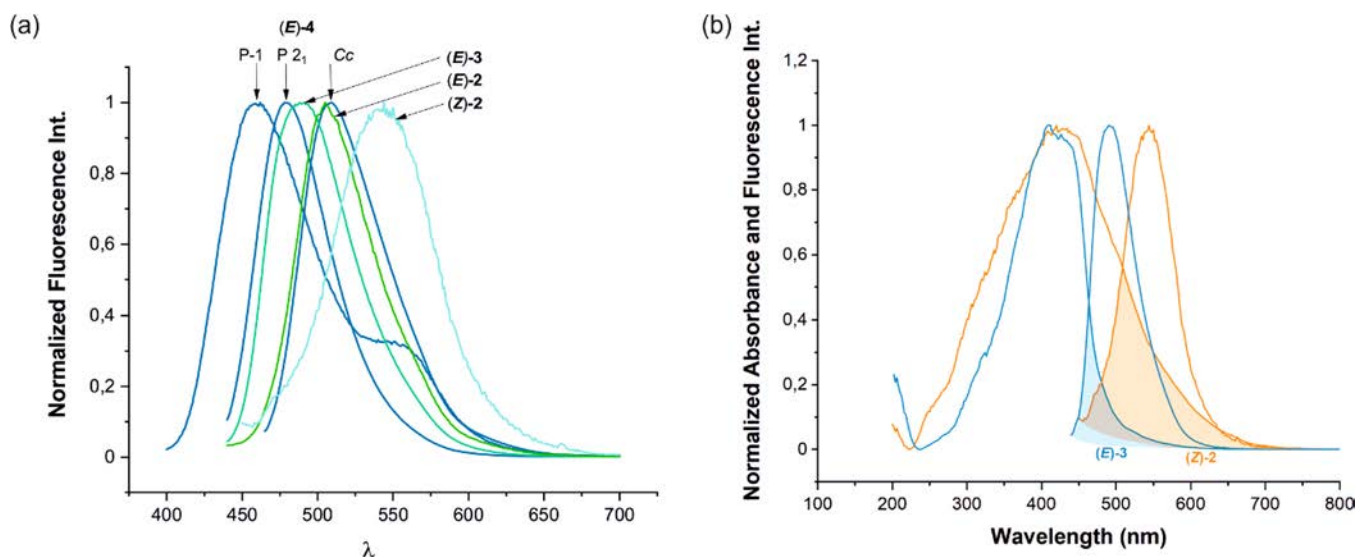


Figure 4. (a) Normalized fluorescence spectra of single crystals. (b) The overlap of the absorption and fluorescence spectra for single crystals of (E)-3 (blue) and (Z)-2 (orange).

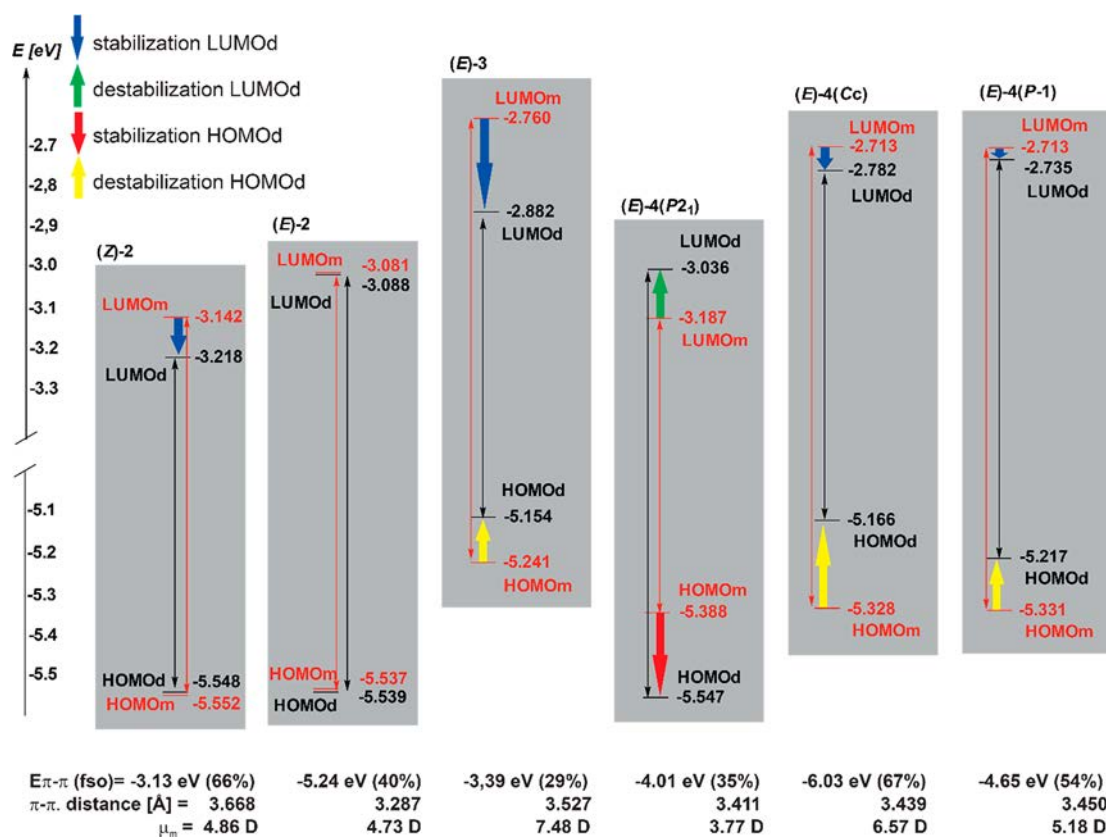


Figure 5. Schematic representation of different energy contributions to the interaction between the studied molecules in dimers or stacks induced by $\pi-\pi$ repulsion, excimer formation, and other interactions, including the $\pi-\pi$ interaction ($E_{\pi-\pi}$ (eV)), the fraction of the $\pi-\pi$ -overlapping surface (fso (%)), the dipole moment for the monomer (μ_m (D)), the HOMO and LUMO for monomer (HOMO_m and LUMO_m, respectively), and the HOMO and LUMO for dimer or stack (HOMO_d and LUMO_d, respectively).

Figure S24a), and for three molecules in the stack is 20.55 D (Table 2 and Figure S11). Similar intramolecular charge transfer was found for head-to-head molecular stacking in the polymorph (E)-4(P₂₁) for which the calculations were performed for two neighboring molecules of the stack. Here, the HOMOs were mainly delocalized over the pyrroloquinoxalin-2-one system of one molecule (including the intra-

molecular hydrogen bond N–H... N_{Qui}), whereas LUMOs were delocalized over the heterocyclic system, including the phenyl ring at C(30), with the exception of the carbonyl group of the second molecule in the stack. The direction of the electron transfer was consistent with the orientation of the dipole moment estimated for one molecule (5.21 D) and for two molecules in the stack (9.83 D, Table 3 and Figure S24b).

However, in the case of stacks in *E*-4(*P*₂₁), the dihedral angle between the phenyl ring and the fluorophore plane is ca. 62°, which causes charge separation in the LUMOs.

In the polymorph (*E*)-4(*P*₁) containing the ethylene linker, the presence of a center of symmetry in the crystal structure causes the same delocalization of the HOMOs over the pyrroloquinoxalin-2-one system on both molecules of the head-to-tail dimer, whereas the LUMOs delocalize over pyrroloquinoxaline and only C(31) of the phenyl ring. In such cases, intramolecular charge transfer occurs within each molecule in the dimer, including the intramolecular hydrogen bond N–H⋯N_{Qui}. In the polymorph (*E*)-4(*C*_c), the dimer is formed by two symmetrically independent molecules of the same chirality in a head-to-tail arrangement, and the delocalization of the HOMOs is similar to the delocalization observed in (*E*)-2 (compare Figure S21 and S23). The LUMO of the dimer of (*E*)-4(*C*_c) unevenly delocalizes into two heterocycles, and the direction of charge transfer is consistent with the orientation of the dimer dipole moment (Figure S26a), with a value of 2.30 D.

The (*E*)-2 single crystal does not contain a linker between the pyridyl group and the pyrroloquinoxaline system, which prevents the formation of an intramolecular hydrogen bond N–H⋯N_{py} and the extension of π -electron coupling. The HOMOs for the (*E*)-2 head-to-tail dimer were delocalized over the pyrroloquinoxaline system, including the intramolecular hydrogen bond N–H⋯N_{Qui} on both molecules of the dimer, whereas the LUMOs were almost delocalized over only one molecule of the dimer, with maximum components on N_{Qui}, C(3), C(30), enamine N(30), the pyridine ring, and the phenyl ring at C(30). Here, DFT calculations indicated that intermolecular charge transfer occurred from both molecules of the dimer to only one component. The (*Z*)-2 single crystals contain a center of symmetry, which causes the same delocalization of the HOMOs over the pyrroloquinoxalin-2-one system and the intramolecular hydrogen bond N–H⋯O=C for both molecules in the dimer, and the LUMOs are delocalized over the pyrroloquinoxaline moiety, the pyridyl ring, and the phenyl ring at C(30).

The HOMO–LUMO gap analysis for the studied monomers shows the influence of the intramolecular hydrogen bonds on the stabilization of the HOMO for the *Z*-isomers (NH⋯O=C) and *E*-isomers (NH⋯N). The formation of hydrogen bonds to the oxygen acceptor (O=C) strongly stabilized the HOMO (−5.552 eV). The difference between the HOMO–LUMO gaps of the monomers and dimers in each case shows the influence of π – π , hydrogen bond, and weak C–H⋯ π interactions, which are present between monomers in the dimer, on the stabilization or destabilization of the dimer in the ground and excited states (Figure 5). The π – π interaction has almost no influence on the stabilization of the HOMO for the (*Z*)-2 and (*E*)-2 dimers. For the *Z*-isomer, there is a moderate stabilization of the excited state due to π – π interactions and excimer formation (note the large fraction, 66%, of π – π overlap). Although the energy of the π – π interactions for (*Z*)-2 and (*E*)-3 is comparable, their quantum yields of fluorescence differ significantly (Table 2). The difference in quantum yields is influenced by the mutual arrangement of the molecules in the (*Z*)-2 dimer and the (*E*)-3 stack. In the dimer, the distance between fluorophore planes is the largest (3.668 Å) among the studied enamine single crystals despite the dipole–dipole interactions as a result of the different conformations of the molecules. A relatively

long interplanar distance in the (*Z*)-2 dimer weakens the π – π interactions. However, the fraction of the superimposition of the molecule surface in the dimer is similar to the fraction of the superimposition of the molecule surface observed in (*E*)-4(*C*_c) (67%). The difference between the fluorescence quenching of single crystals of (*Z*)-2 and that of (*E*)-3 is caused by the reabsorption of re-emitted photons⁵³ (see the overlap of the normalized absorption and fluorescence spectra for the single crystals in Figure 4b). For the (*E*)-4(*C*_c) polymorph, the greatest destabilization of the HOMO induced by π – π repulsion (by 0.169 eV) and the relatively small stabilization of the LUMO (0.069 eV) were found, which may result from both π – π and C–H⋯ π interactions between the A and B molecules in the dimer (C(43B)–H(43B)⋯Cg4(A) = 0.95, 2.58, and 3.392 Å and 162°, where Cg4(A) is the center of gravity of the phenyl ring at N(1A))⁴⁵. The HOMO–LUMO gap for the AB dimer is 0.231 eV lower in relation to the monomer HOMO–LUMO gap, which enables charge transfer between A and B molecules in the dimer. In the case of (*E*)-3, the π – π interaction energy of the dimer and the surface area of the fluorophore overlap are relatively small (−3.39 kcal/mol and 29%, respectively). The HOMO is destabilized by 0.0096 eV, whereas the LUMO is highly stabilized by 0.122 eV; thus, the HOMO–LUMO gap for the dimer decreases by approximately 0.209 eV. Therefore, the stabilization of the dimer in the excited state is influenced mainly by excimer formation that is amplified by the C–H⋯N interaction (C(12)–H(12)⋯N9(*x*, *y* − 1, *z*) = 0.93, 2.69, and 3.633 Å and 177°). A small HOMO–LUMO gap enables intermolecular charge transfer between molecules in the stack. For (*E*)-4(*P*₂₁), the polymorph that exhibits helical chirality, the HOMO is stabilized by 0.159 eV and the LUMO is destabilized by 0.151 eV. The HOMO–LUMO gap for the dimer increased by approximately 0.300 eV. In these cases, the weak overlap between the absorption and emission spectra and the large Stokes shift of 4104 cm^{−1} prevent reabsorption.

In this case, the water molecule stabilized the ground-state bridging two neighboring molecules in the stack due to the hydrogen bond [(O45–H451⋯O2 = 0.91, 1.98, and 2.809 Å and 151°) and the interaction of its lone pair with the pyrrole ring (O45⋯Cg1(*x* + 1, *y*, *z*) = 3.134 Å). For (*E*)-4(*P*₁), the destabilizing effect of π – π interactions was observed for the HOMO, whereas their influence on LUMO stabilization was very small. In this case, the reabsorption phenomenon is present due to the centrosymmetric relationship between the two molecules forming dimers and the 54% fraction of π – π overlapping surfaces.

CONCLUSIONS

The length of the linker (CH₂)_{*n*} (*n* = 0, 1, or 2) between the enamino-pyrroloquinoxaline system and the pyridyl group influences the general shape of assembling molecules and the packing of the molecules in the crystal structures. Each of the studied enamino-pyrrolo[2,3-*b*]quinoxaline derivatives exhibits a permanent dipole moment. The reorientation of the molecular permanent dipole moment in some cases is caused by an additional intramolecular hydrogen bond interaction (N–H⋯N_{py} apart from N–H⋯N_{Qui}) that affects the conformation of the molecules.

The mutual orientation of the fluorophores in dimers or stacks is induced by dipole–dipole interactions. We have shown the significant influence of the methylene linker on the formation of intramolecular bifurcated hydrogen bonds,

favoring the coplanarity of the pyridyl ring with the fluorophore and causing the extension of π -electron coupling between these moieties.

For enamino-pyrrolo[2,3-*b*]quinoxaline derivatives, two mechanisms of intra- and intermolecular charge transfer are responsible for the fluorescence properties of the single crystals. Crystals that contain centrosymmetric dimers exhibit 1 quantum fluorescence yields (Φ_f) lower than those of crystals containing stacks of molecules in translational arrangements or noncentrosymmetric dimers. The highest Φ_f values were observed for the (*E*)-3 and (*E*)-4(*P*₂) crystals containing stacks of molecules and (*E*)-4(*Cc*), where the dimer was formed by two molecules of the same chirality in a head-to-tail arrangement.

The calculated frontier orbitals (HOMO and LUMO) and deformation densities indicate that the intermolecular charge transfer, which was observed for crystals containing stacks of translationally arranged enamino-pyrrolo[2,3-*b*]quinoxaline molecules or noncentrosymmetric dimers, influenced the fluorescence properties of the molecules in the crystalline state. In the case of centrosymmetric dimers, DFT calculations elucidate intramolecular charge transfer within each molecule of the dimer.

■ ASSOCIATED CONTENT

SI Supporting Information

The Supporting Information is available free of charge at <https://pubs.acs.org/doi/10.1021/acs.cgd.1c00947>.

Scheme of synthesis and *E/Z* isomerization of enamines; ¹H NMR, fluorescence, UV–vis, and IR spectra of enamines; crystal structure data, fluorescence quantum yields; fluorescence lifetimes; DFT calculations; and QTAIM analysis (PDF)

Accession Codes

CCDC 1519234 and 2086613 contain the supplementary crystallographic data for this paper. These data can be obtained free of charge via www.ccdc.cam.ac.uk/data_request/cif, or by emailing data_request@ccdc.cam.ac.uk, or by contacting The Cambridge Crystallographic Data Centre, 12 Union Road, Cambridge CB2 1EZ, UK; fax: +44 1223 336033.

■ AUTHOR INFORMATION

Corresponding Author

Katarzyna Ostrowska – Faculty of Chemistry, Jagiellonian University, PL-30387 Kraków, Poland; orcid.org/0000-0002-6425-5331; Email: ostrowsk@chemia.uj.edu.pl; Fax: +48-12-68-62-750

Authors

Katarzyna M. Stadnicka – Faculty of Chemistry, Jagiellonian University, PL-30387 Kraków, Poland; orcid.org/0000-0002-3898-5824

Marlena Gryl – Faculty of Chemistry, Jagiellonian University, PL-30387 Kraków, Poland; orcid.org/0000-0003-2267-1588

Oskar Klimas – Faculty of Chemistry, Jagiellonian University, PL-30387 Kraków, Poland

Mateusz Z. Brela – Faculty of Chemistry, Jagiellonian University, PL-30387 Kraków, Poland; orcid.org/0000-0002-4686-5400

Piotr Goszczycki – Faculty of Chemistry, Jagiellonian University, PL-30387 Kraków, Poland

Michał Liberka – Faculty of Chemistry, Jagiellonian University, PL-30387 Kraków, Poland; orcid.org/0000-0002-8102-1801

Jarosław Grolik – Faculty of Chemistry, Jagiellonian University, PL-30387 Kraków, Poland

Agnieszka Węgrzyn – Faculty of Chemistry, Jagiellonian University, PL-30387 Kraków, Poland; orcid.org/0000-0002-9835-9825

Complete contact information is available at: <https://pubs.acs.org/doi/10.1021/acs.cgd.1c00947>

Author Contributions

Crystal structure determination was done by K. M. Stadnicka. The manuscript was written through contributions of all authors. All authors have given approval to the final version of the manuscript.

Notes

The authors declare no competing financial interest.

■ ACKNOWLEDGMENTS

The results of DFT calculations presented in this paper were obtained using PL-Grid infrastructure and resources provided by ACC Cyfronet AGH.

■ REFERENCES

- (1) Varghese, Sh.; Das, S. Role of Molecular Packing in Determining Solid-State Optical Properties of π -Conjugated Materials. *J. Phys. Chem. Lett.* **2011**, *2* (8), 863–873.
- (2) Varughese, S. Non-covalent routes to tune the optical properties of molecular materials. *J. Mater. Chem. C* **2014**, *2*, 3499–3516.
- (3) Wang, Ch.; Dong, H.; Jiang, L.; Hu, W. Organic Semiconductor Crystals. *Chem. Soc. Rev.* **2018**, *47*, 422–500.
- (4) Park, S. K.; Kim, J. H.; Park, S. Y. Organic 2D Optoelectronic Crystals: Charge Transport, Emerging Functions, and Their Design Perspective. *Adv. Mater.* **2018**, *30* (42), 1704759.
- (5) Kitaigorodsky, A. I. *Molecular Crystals and Molecules*; Academic Press: New York, NY, 1973.
- (6) Corpinot, M. K.; Bučar, D.-K. A. Practical Guide to the Design of Molecular Crystals. *Cryst. Growth Des.* **2019**, *19* (2), 1426–1453.
- (7) Desiraju, G. R.; Steiner, T. *The Weak Hydrogen Bond In Structural Chemistry and Biology*; Oxford University Press: Oxford, U.K., 2006.
- (8) Wang, Y.; Hasegawa, T.; Matsumoto, H.; Michinobu, T. Significant Improvement of Unipolar n-Type Transistor Performances by Manipulating the Coplanar Backbone Conformation of Electron-Deficient Polymers via Hydrogen Bonding. *J. Am. Chem. Soc.* **2019**, *141* (8), 3566–3575.
- (9) Wu, H.; Wang, Sh.; Ding, J.; Wang, R.; Zhang, Y. Effect of π -conjugation on solid-state fluorescence in highly planar dyes bearing an intramolecular H-bond. *Dyes Pigm.* **2020**, *182*, 108665.
- (10) London, F. The general theory of molecular forces. *Trans. Faraday Soc.* **1937**, *33*, 8b–26.
- (11) Hunter, Ch. A.; Sanders, J. K. M. The nature of π - π interaction. *J. Am. Chem. Soc.* **1990**, *112* (14), 5525–5534.
- (12) Sinnokrot, M. O.; Sherrill, C. D. Unexpected Substituent Effects in Face-to-Face π -Stacking Interactions. *J. Phys. Chem. A* **2003**, *107* (41), 8377–8379.
- (13) Huber, R. G.; Margreiter, M. A.; Fuchs, J. E.; von Grafenstein, S.; Tautermann, Ch. S.; Liedl, K. R.; Fox, T. Heteroaromatic π -Stacking Energy Landscapes. *J. Chem. Inf. Model.* **2014**, *54* (5), 1371–1379.
- (14) Wheeler, S. E. Local Nature of Substituent Effects in Stacking Interactions. *J. Am. Chem. Soc.* **2011**, *133* (26), 10262–10274.
- (15) Janiak, Ch. A critical account on π -stacking in metal complexes with aromatic nitrogen-containing ligands. *J. Chem. Soc., Dalton Trans.* **2000**, 3885–3896.

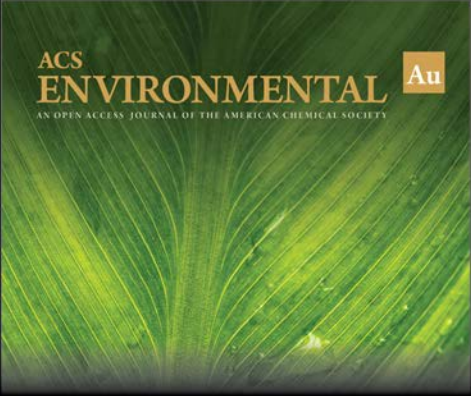
- (16) Margenau, H.; Kestner, N. *Theory of intermolecular forces*; International Series of Monographs in Natural Philosophy; Pergamon Press: Oxford, U.K., 1969.
- (17) Srujana, P.; Sudhakar, P.; Radhakrishnan, T. P. Enhancement of fluorescence efficiency from molecules to materials and the critical role of molecular assembly. *J. Mater. Chem. C* **2018**, *6* (35), 9314–9329.
- (18) Goszczycki, P.; Stadnicka, K.; Brela, M. Z.; Grolik, J. I.; Ostrowska, K. Synthesis, crystal structures, and optical properties of the π - π interacting pyrrolo[2,3-*b*]quinoxaline derivatives containing 2-thienyl substituent. *J. Mol. Struct.* **2017**, *1146*, 337–346.
- (19) Frisch, M. J.; Trucks, G. W.; Schlegel, H. B.; Scuseria, G. E.; Robb, M. A.; Cheeseman, J. R.; Scalmani, G.; Barone, V.; Petersson, G. A.; Nakatsuji, H.; Li, X.; Caricato, M.; Marenich, A. V.; Bloino, J.; Janesko, B. G.; Gomperts, R.; Mennucci, B.; Hratchian, H. P.; Ortiz, J. V.; Izmaylov, A. F.; Sonnenberg, J. L.; Williams-Young, D.; Ding, F.; Lipparini, F.; Egidi, F.; Goings, J.; Peng, B.; Petrone, A.; Henderson, T.; Ranasinghe, D.; Zakrzewski, V. G.; Gao, J.; Rega, N.; Zheng, G.; Liang, W.; Hada, M.; Ehara, M.; Toyota, K.; Fukuda, R.; Hasegawa, J.; Ishida, M.; Nakajima, T.; Honda, Y.; Kitao, O.; Nakai, H.; Vreven, T.; Throssell, K.; Montgomery, J. A., Jr.; Peralta, J. E.; Ogliaro, F.; Bearpark, M. J.; Heyd, J. J.; Brothers, E. N.; Kudin, K. N.; Staroverov, V. N.; Keith, T. A.; Kobayashi, R.; Normand, J.; Raghavachari, K.; Rendell, A. P.; Burant, J. C.; Iyengar, S. S.; Tomasi, J.; Cossi, M.; Millam, J. M.; Klene, M.; Adamo, C.; Cammi, R.; Ochterski, J. W.; Martin, R. L.; Morokuma, K.; Farkas, O.; Foresman, J. B.; Fox, D. J. *Gaussian 16*, rev. C.01; Gaussian, Inc.: Wallingford, CT, 2016.
- (20) Bader, R. F. W. *Atoms in Molecules. A Quantum Theory*; Clarendon Press: Oxford, UK, 1990.
- (21) Todd, A.; Keith, T. K. *AIMAll*, ver. 19.10.12; Gristmill Software, Overland Park, KS, 2019. aim.tkgristmill.com.
- (22) *CrysAlisPro*, ver. 1.171.40.14e; Rigaku: Tokyo, Japan, 2018.
- (23) Altomare, A.; Casciaro, G.; Giacovazzo, C.; Guagliardi, A.; Burla, M. C.; Polidori, G.; Camalli, M. *SIR92* - A program for automatic solution of crystal structures by direct methods. *J. Appl. Crystallogr.* **1994**, *27*, 435.
- (24) Sheldrick, G. M. Crystal structure refinement with SHELXL. *Acta Crystallogr. Sect. C* **2015**, *71*, 3–8.
- (25) Farrugia, L. J. ORTEP-3 for Windows - a version of ORTEP-III with a Graphical User Interface (GUI). *J. Appl. Crystallogr.* **1997**, *30*, 565.
- (26) Farrugia, L. J. WinGX suite for small-molecule single-crystal crystallography. *J. Appl. Crystallogr.* **1999**, *32*, 837–838.
- (27) Macrae, C. F.; Edgington, P. R.; McCabe, P.; Pidcock, G.; Shields, P.; Taylor, R.; Towler, M.; van de Streek, J. Mercury: visualization and analysis of crystal structures. *J. Appl. Crystallogr.* **2006**, *39*, 453–457.
- (28) te Velde, G.; Bickelhaupt, F. M.; Baerends, E. J.; Guerra, C. F.; van Gisbergen, S. J. A.; Snijders, J. G.; Ziegler, T. Chemistry with ADF. *J. Comput. Chem.* **2001**, *22* (9), 931–936.
- (29) Becke, A. Density-functional exchange-energy approximation with correct asymptotic behavior. *Phys. Rev. A* **1988**, *38* (6), 3098.
- (30) Perdew, J. Density-functional approximation for the correlation energy of the inhomogeneous electron gas. *Phys. Rev. B* **1986**, *33* (12), 8822.
- (31) Grimme, S.; Ehrlich, S.; Goerigk, L. Effect of the damping function in dispersion corrected density functional theory. *J. Comput. Chem.* **2011**, *32* (7), 1456.
- (32) van Lenthe, E.; Baerends, E. J.; Snijders, J. G. Relativistic total energy using regular approximations. *J. Chem. Phys.* **1994**, *101*, 9783.
- (33) (a) Ziegler, T.; Rauk, A. Carbon monoxide, carbon monosulfide, molecular nitrogen, phosphorus trifluoride, and methyl isocyanide as σ donors and π acceptors. A theoretical study by the Hartree-Fock-Slater transition-state method. *Inorg. Chem.* **1979**, *18* (7), 1755–1759. (b) Ziegler, T.; Rauk, A. A theoretical study of the ethylene-metal bond in complexes between copper(1+), silver(1+), gold(1+), platinum(0) or platinum(2+) and ethylene, based on the Hartree-Fock-Slater transition-state method. *Inorg. Chem.* **1979**, *18* (6), 1558–1565.
- (34) Mitoraj, M.; Michalak, A.; Ziegler, T. A Combined Charge and Energy Decomposition Scheme for Bond Analysis. *J. Chem. Theory Comput.* **2009**, *5* (4), 962–975.
- (35) van Gisbergen, S. J. A.; Kootstra, F.; Schipper, P. R. T.; Gritsenko, O. V.; Snijders, J. G.; Baerends, E. J. Density-functional-theory response-property calculations with accurate exchange-correlation potentials. *Phys. Rev. A* **1998**, *57*, 2556.
- (36) van Gisbergen, S. J. A.; Rosa, A.; Ricciardi, G.; Baerends, E. J. Time-dependent density functional calculations on the electronic absorption spectrum of free base porphyrin. *J. Chem. Phys.* **1999**, *111*, 2499.
- (37) Martin, R. L. Natural transition orbitals. *J. Chem. Phys.* **2003**, *118*, 4775.
- (38) Hutter, J.; Iannuzzi, M.; Schiffrmann, F.; VandeVondele, J. CP2K: atomistic simulations of condensed matter systems, WIREs. *Comput. Mol. Sci.* **2014**, *4* (1), 15–25.
- (39) Iannuzzi, M.; Chassaing, T.; Wallman, T.; Hutter, J. Ground and excited state density functional calculations with the Gaussian and augmented-plane-wave method. *CHIMIA International Journal for Chemistry* **2005**, *59* (7–8), 499–503.
- (40) Becke, A. D. Density-functional thermochemistry. III. The role of exact exchange. *J. Chem. Phys.* **1993**, *98* (7), 5648–5652.
- (41) Lee, C.; Yang, W.; Parr, R. G. Development of the Colle-Salvetti correlation-energy formula into a functional of the electron density. *Phys. Rev. B* **1988**, *37* (2), 785–789.
- (42) Humphrey, W.; Dalke, A.; Schulten, K. VMD: visual molecular dynamics. *J. Mol. Graph.* **1996**, *14* (1), 33–38.
- (43) Ostrowska, K.; Musielak, B.; Szneler, E.; Dudek, Ł.; Gryl, M.; Stadnicka, K. Chelate Ring Size Effect as a Factor of Selective Fluorescent Recognition of Zn²⁺ Ions by Pyrrolo[2,3-*b*]quinoxaline with a Substituted 2-Pyridyl Group Receptor. *Inorg. Chem.* **2015**, *54* (17), 8423–8435.
- (44) Ostrowska, K.; Stadnicka, K.; Gryl, M.; Musielak, B.; Witek, Ł. J.; Bochenska, O. Synthesis, structure, and photophysical properties of luminescent zinc and cadmium complexes containing 2-pyridyl-substituted pyrrolo[2,3-*b*]quinoxaline. *Polyhedron* **2017**, *133* (5), 294–301.
- (45) Ostrowska, K.; Dudek, Ł.; Grolik, J.; Gryl, M.; Stadnicka, K. Pyrrolo[2,3-*b*]quinoxaline with 2-(2-aminoethyl) pyridine chain highly selective fluorescent receptor for Zn²⁺ exhibiting a dual fluorescence and AIEE in crystalline state. *CrystEngComm* **2015**, *17* (3), 498–502.
- (46) Ostrowska, K.; Piegza, E.; Rapala-Kozik, M.; Stadnicka, K. Efficient *N*-Alkyl Enamination of 3-(Thiobenzoyl)pyrrolo[2,3-*b*]quinoxalin-2-one, *E/Z* Isomerisation of the Reaction Products and Potential Fluorescent Sensors for Zinc(II) Ion. *Eur. J. Org. Chem.* **2012**, *2012* (19), 3636–3646.
- (47) Wentrup, C.; Koch, R.; Kleinpeter, E. Twisted C=C Double Bonds with Very Low Rotational Barriers in Dioxanones and Isoxazolones Determined by Low-Temperature Dynamic NMR Spectroscopy and Computational Chemistry. *Eur. J. Org. Chem.* **2016**, *2016* (29), 4985–4990.
- (48) Olyaei, A.; Javarsineh, S.; Sadeghpour, M. Green synthesis and *Z/E*-isomerization of novel coumarin enamines induced by organic solvents. *Chem. Heterocycl. Compd.* **2018**, *54* (10), 934–939.
- (49) Vollmer, F.; Rettig, W.; Birckner, E. Photochemical Mechanisms Producing Large Fluorescence Stokes Shifts. *J. Fluoresc.* **1994**, *4* (1), 65–69.
- (50) Cruz-Cabeza, A. J.; Bernstein, J. Conformational Polymorphism. *Chem. Rev.* **2014**, *114* (4), 2170–2191.
- (51) (a) Cahn, R. S.; Ingold, C. K.; Prelog, V. The Specification of Asymmetric Configuration in Organic Chemistry. *Experientia* **1956**, *12*, 81–94. (b) Cahn, R. S.; Ingold, C. K.; Prelog, V. Specification of Molecular Chirality. *Angew. Chem. Internat. Ed.* **1966**, *5* (5), 385–415.
- (52) Espinosa, E.; Molins, E.; Lecomte, C. Hydrogen bond strengths revealed by topological analyses of experimentally observed electron densities. *Chem. Phys. Lett.* **1998**, *285*, 170–173.
- (53) Schillmoller, T.; Herbst-Irmer, R.; Stalke, D. Insights into Excimer Formation Factors from Detailed Structural and Photo-

physical Studies in the Solid-State. *Adv. Optical Mater.* **2021**, *9*, 2001814.

(54) Liu, Y. S.; de Mayo, P.; Ware, W. R. Photophysics of polycyclic aromatic hydrocarbons adsorbed on silica gel surfaces. 3. Fluorescence quantum yields and radiative decay rate constants derived from lifetime distributions. *J. Phys. Chem.* **1993**, *97*, 5995–6001.

(55) Patra, A.; Hebalkar, N.; Sreedhar, B.; Sarkar, M.; Samanta, A.; Radhakrishnan, T. P. Tuning the Size and Optical Properties in Molecular Nano/Microcrystals: Manifestation of Hierarchical Interactions. *Small* **2006**, *2* (5), 650–659.


(56) Katoh, R.; Suzuki, K.; Furube, A.; Kotani, M.; Tokumaru, A. Fluorescence Quantum Yield of Aromatic Hydrocarbon Crystals. *J. Phys. Chem. C* **2009**, *113* (7), 2961–2965.




ACS
ENVIRONMENTAL Au
AN OPEN ACCESS JOURNAL OF THE AMERICAN CHEMICAL SOCIETY

Editor-in-Chief: **Prof. Shelley D. Minteer**, University of Utah, USA

Deputy Editor:
Prof. Xiang-Dong Li
Hong Kong Polytechnic University, China

Open for Submissions 

pubs.acs.org/environau  ACS Publications
Most Trusted. Most Cited. Most Read.